ADVANCED FUNCTIONAL MATERIALS
www.afm-journal.de

www.MaterialsViews.com

Smart Hybrids of Zn_2GeO_4 Nanoparticles and Ultrathin g-C_3N_4 Layers: Synergistic Lithium Storage and Excellent Electrochemical Performance

Xiaodan Li, Yi Feng, Meicheng Li, Wei Li, Hao Wei, and Dandan Song*

Smart hybrids of Zn_2GeO_4 nanoparticles and ultrathin g-C_3N_4 layers (Zn_2GeO_4/g-C_3N_4 hybrids) are realized by a facile solution approach, where g-C_3N_4 layers act as an effective substrate for the nucleation and subsequent in situ growth of Zn_2GeO_4 nanoparticles. A synergistic effect is demonstrated on the two building blocks of Zn_2GeO_4/g-C_3N_4 hybrids for lithium storage: Zn_2GeO_4 nanoparticles contribute high capacity and serve as spacers to isolate the ultrathin g-C_3N_4 layers from restacking, resulting in expanded interlayer and exposed vacancies with doubly bonded nitrogen for extra Li-ion storage and diffusion pathway; 2D g-C_3N_4 layers, in turn, minimize the strain of particles expansion and prevent the formation of unstable solid electrolyte interphase, leading to highly reversible lithium storage. Benefiting from the remarkable synergy, the Zn_2GeO_4/g-C_3N_4 hybrids exhibit highly reversible capacity of 1370 mA h g^{-1} at 200 mA g^{-1} after 140 cycles and excellent rate capability of 950 mA h g^{-1} at 2000 mA g^{-1}. The synergistic effect originating from the hybrids brings out excellent electrochemical performance, and thus casts new light on the development of high-energy and high-power anode materials.

1. Introduction

Nowadays, the energy crises and environmental pollution deriving from the overdependence of fossil fuels have inspired the worldwide attention to hybrid electric vehicles and renewable energy. The developments of future hybrid electric vehicles and renewable energy storage rely heavily on the high-energy and high-power density Li-ion batteries (LIBs).[1–4] However, current commercialized graphite anodes suffer from low energy density (372 mA h g^{-1}),[5] which cannot meet the demand of next-generation, high-energy, and high-power LIBs. Therefore, significant research efforts have been devoted to searching alternative anode materials, such as Si,[6] Ge,[7] and their oxides[8–10] to solve the contradictions. Among these alternatives, Ge and its oxides are expected to act as both high-energy and high-power anodes due to the unique, fascinating features of Ge such as the relatively high theoretical specific capacity of 1600 mA h g^{-1}, high conductivity, and fast lithium-ion diffusivity.[11,12] In particularly, nanostructured Ge-based ternary oxides also have advantages of low cost, moderate volume change, and more importantly, enhanced electrical conductivity originated from a conductive matrix formed by Ge and the second metal,[13–17] which makes nanostructured Ge-based ternary oxides to be competitive candidates for high-performance LIBs.[18] Despite the merits mentioned above, nanostructured Ge-based ternary oxides suffer from two detrimental deficiencies which prohibit their practical applications: agglomeration and volume changes during lithiation/delithiation processes. To overcome these obstacles, a universal strategy is to immobilize active materials into/onto substrate matrices to construct composites.[19–24] It is believed that such immobilization or embedment can greatly limit the agglomeration of nanoparticles and accommodate the volume expansion during the charge–discharge processes, then higher specific capacity and better cycling performance could be achieved.

Recently, it has been reported that pyrrolic N "hole" defect should be responsible for the high rate capability and high capacity of N-doped graphene due to short-distance orderings formed on edges and profound surface defects during discharging.[25] Opportunely, the natural structure of graphitic carbon nitride (g-C_3N_4) contains large amount of pyrrolic N "hole" defect in the lattice and doubly bonded nitrogen at the edges of the vacancy, which are beneficial for the adsorption and diffusion of lithium ion;[26–29] meanwhile, g-C_3N_4 is inexpensive and nontoxic, and can be rapidly synthesized by the facile and scalable heating method,[30,31] avoiding the tedious pretreatment, multisteps, large quantities of toxic oxidants or reductants which are necessary for graphene preparation. On

X. Li, Prof. M. Li, D. Song
State Key Laboratory of Alternate Electrical Power System with Renewable Energy Sources
North China Electric Power University
Beijing 102206, P. R. China
E-mail: mcli@ncepu.edu.cn
Y. Feng
Department of Chemical Engineering
Monash University
Clayton, Victoria 3800, Australia
W. Li
International Iberian Nanotechnology Laboratory (INL)
Braga 4715-330, Portugal
H. Wei
PFPC
School of Chemistry
The University of Melbourne
Melbourne, Victoria 3010, Australia

DOI: 10.1002/adfm.201502938

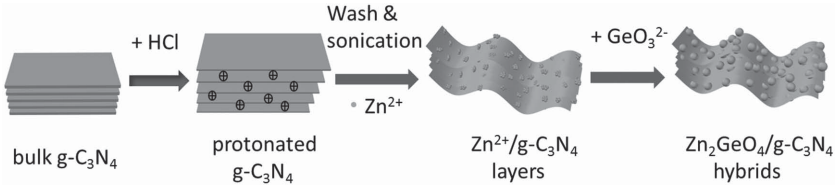

Figure 1. Illustration of the synthesis process of the Zn_2GeO_4/g-C_3N_4 hybrids.

the other hand, in order to adequately expose pyrrolic N "hole" defect of g-C_3N_4 for lithium storage, it is suitable to immobilize nanoparticles into g-C_3N_4, where nanoparticles serve as spacers to isolate g-C_3N_4 layers. Zn_2GeO_4 nanoparticle is one of the most promising candidates among various Ge-based materials, because a) ZnO has a high capacity for lithium storage and b) the mass percentage of Ge in Zn_2GeO_4 is only 27%, much lower than that in other Ge-based materials, lowering the cost. On the basis of above conception, we propose and design Zn_2GeO_4/g-C_3N_4 hybrids as high-performance anode materials for LIBs, where Zn_2GeO_4 nanoparticles would be immobilized into large-area g-C_3N_4 and act as spacers to isolate ultrathin g-C_3N_4 layers. In this case, the advantages of Zn_2GeO_4 (high conductivity, high capacity) and g-C_3N_4 (large-area scaffold, pyrrolic N "hole" defects) are expected to be integrated within this hybrid system, resulting in complementary and synergistic effect.

In this study, the Zn_2GeO_4/g-C_3N_4 hybrids have been successfully synthesized by a facile, low-cost, and scalable solution approach, which exhibit the synergistic effect on their lithium storage. The Zn_2GeO_4 nanoparticles were grown in situ between/on large-area g-C_3N_4 to isolate ultrathin g-C_3N_4 layers from restacking and expand the interlayer of g-C_3N_4 layers. Benefiting from the remarkable synergy, the Zn_2GeO_4/g-C_3N_4 hybrids exhibited highly reversible capacity of 1370 mA h g^{-1} at 200 mA g^{-1} after 140 cycles and excellent rate capability of 950 mA h g^{-1} at 2000 mA g^{-1}. The synergistic strategy of Zn_2GeO_4/g-C_3N_4 hybrids could be applied to guide the rational design of similar hybrid system, such as SnO_2/g-C_3N_4 and Co_3O_4/g-C_3N_4, as promising anode materials for high-performance lithium ion batteries.

2. Results and Discussion

In order to realize the Zn_2GeO_4/g-C_3N_4 hybrids, Zn_2GeO_4 NPs were encapsulated by large-area g-C_3N_4 layers via a facile, low-cost, and scalable solution approach, as illustrated by **Figure 1**. First, the g-C_3N_4 bulk was protonated in the HCl solution to promote the exfoliation of g-C_3N_4 bulk into layers under ultrasonication, providing large-area scaffold for the hybridization with Zn_2GeO_4 NPs. Then, the g-C_3N_4 layers were washed and dispersed in deionized (DI) water. With the addition of $Zn(CH_3COO)_2 \cdot 2H_2O$, free Zn^{2+} were electrostatically adhered onto the surface of g-C_3N_4 layers. And the size of pyrrolic N "holes" defect on g-C_3N_4 layers is much bigger than that of ion, so they may provide more pathways for the diffusion of ions. When GeO_3^{2-} species were added, the gradually formed Zn_2GeO_4 nanoparticles, as shown in Equations (1)–(4), could act as spacers to further expand the interlayers of g-C_3N_4 layer and isolate these ultrathin layers. At last, Zn_2GeO_4 nanoparticles were encapsulated by large-area g-C_3N_4 layers after removal of the moisture

$$GeO_3^{2-} + H_2O \rightarrow HGeO_3^- + OH^- \quad (1)$$

$$HGeO_3^- + H_3O^+ \rightarrow Ge(OH)_4 \quad (2)$$

$$Zn^{2+} + 2OH^- \rightarrow Zn(OH)_2 \quad (3)$$

$$2Zn(OH)_2 + Ge(OH)_4 \rightarrow Zn_2GeO_4 + 4H_2O \quad (4)$$

The crystal structures and composition of the as-prepared samples were examined by X-ray diffraction (XRD), as shown in **Figure 2**a. The XRD pattern of g-C_3N_4 presents a main diffraction peak at 27.4°, which indicates that the as-prepared g-C_3N_4 is graphite-like carbon nitride plates with exposed (001) surfaces.[32] The diffraction peaks of the as-prepared Zn_2GeO_4 NPs can be assigned to rhombohedral Zn_2GeO_4 (JCPDS No. 11-0687) with lattice constants $a = b = 1.423$ nm, $c = 0.953$ nm, $\alpha = \beta = 90°$, and $\gamma = 120°$. In the XRD pattern of hybrids, an obvious (001) diffraction peak of g-C_3N_4 appeared except the standard peaks of Zn_2GeO_4, demonstrating that the as-prepared hybrids are a mixture of graphite-like carbon nitride (g-C_3N_4) and rhombohedral Zn_2GeO_4.

In the typical Zn_2GeO_4/g-C_3N_4 hybrids, we found that large amounts of nanoparticles are homogeneously encapsulated by large-area g-C_3N_4 layers, as shown in Figure 2b. From a magnification image in Figure 2c, it is revealed that Zn_2GeO_4

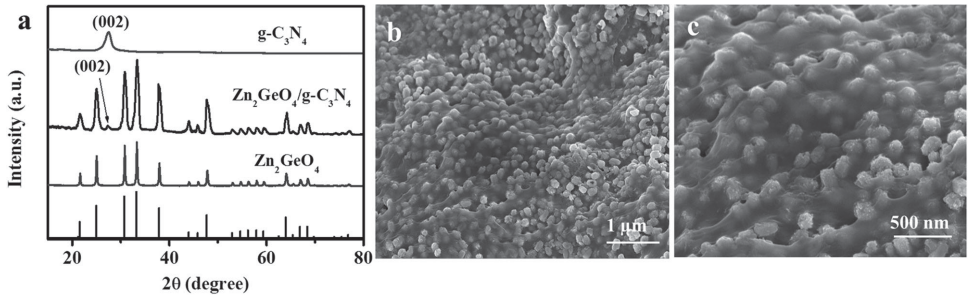

Figure 2. Composition and morphology characterization. a) XRD patterns of bare g-C_3N_4, Zn_2GeO_4/g-C_3N_{4-10}, and pure Zn_2GeO_4 NPs and standard pattern of JCPDS Card No. 11-0687. b) Low- and c) high-magnification SEM images of Zn_2GeO_4/g-C_3N_{4-10}.

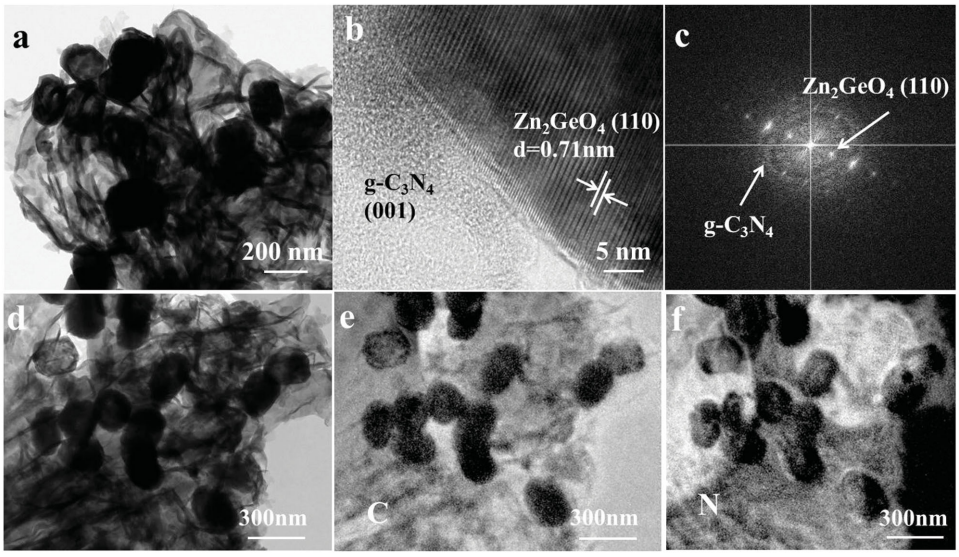

Figure 3. Detailed structural characterization. a) TEM image of Zn_2GeO_4/g-C_3N_{4-10}, b,c) HRTEM and corresponding FFT pattern of the hybrids, respectively, and d) TEM image of Zn_2GeO_4/g-C_3N_{4-10} and the corresponding electron spectroscopic images of e) carbon and f) nitrogen. The element content increases from dark color to light color.

nanoparticles in the hybrids are 100–200 nm in diameter. And the large-area g-C_3N_4 layers are wrinkled. The wrinkled feature of g-C_3N_4 layers in the hybrids is due to the flexibility of ultrathin g-C_3N_4 layers isolated by Zn_2GeO_4 nanoparticles, whereas g-C_3N_4 bulk is very hard. Different mass ratios of Zn_2GeO_4 and g-C_3N_4 were also prepared (Figure S1a,b, Supporting Information), whereas only an optimal ratio (Zn_2GeO_4/g-C_3N_{4-10}, Figure 2b,c) enables the maintenance of ultrathin g-C_3N_4 layers and well-dispersed nanoparticles in the hybrids. The Zn_2GeO_4/g-C_3N_4 hybrids with excess g-C_3N_4 (Zn_2GeO_4/g-C_3N_{4-30}, shown in Figure S1b, Supporting Information) present thickened and restacked g-C_3N_4 layers. **Figure 3**a and Figure S1e (Supporting Information) show a typical transmission electron microscopy (TEM) image of the Zn_2GeO_4/g-C_3N_4 hybrids. It can be seen that Zn_2GeO_4 nanoparticles grew in situ on the outer surface of g-C_3N_4 layers and in the interlayer of the g-C_3N_4 layers. The former are tightly anchored on the g-C_3N_4 layers and the latter could be regarded to be intercalated/embedded into the g-C_3N_4 layers. Thus, the agglomeration of particles is suppressed due to the existence of g-C_3N_4 layers compared to pure Zn_2GeO_4 NPs (Figure S1c, Supporting Information). For the pure Zn_2GeO_4 NPs, the high-resolution TEM (HRTEM) images (Figure S1d, Supporting Information) show lattice fringes with a spacing of 0.28 nm, corresponding to the (113) plane of rhombohedral Zn_2GeO_4. When hybridized with g-C_3N_4 layers, Zn_2GeO_4 NPs expose the (110) plane with a lattice spacing of 0.71 nm (Figure 3b) except (113) plane (Figure S1e,f, Supporting Information). Thus, a Zn_2GeO_4 (110)/g-C_3N_4 (001) heterojunction interface was formed,[32] which demonstrates that the g-C_3N_4 substrate has effect on the in situ growth of Zn_2GeO_4. The corresponding fast Fourier transform (FFT) pattern (Figure 3c) of the Zn_2GeO_4/g-C_3N_{4-10} suggests that each crystalline region of Zn_2GeO_4 NPs is composed of a single crystalline domain while g-C_3N_4 was polycrystalline.[22] Furthermore, electron spectroscopic images of Zn_2GeO_4/g-C_3N_4 show that the C and N elements mainly contribute to the formation of matrix part in these hybrids, demonstrating the hybridization of Zn_2GeO_4 NPs and ultrathin g-C_3N_4 layers.

The chemical states of elements on the surface of Zn_2GeO_4/g-C_3N_{4-10} were investigated by X-ray photoelectron spectroscopy (XPS). The high-resolution XPS spectra (**Figure 4**a–c) show that the binding energies of Zn $2p_{1/2}$, Zn $2p_{3/2}$, Ge 3d, and O 1s peaks in the Zn_2GeO_4/g-C_3N_{4-10} are located at 1045, 1022, 32, and 531.2 eV, respectively, which are consistent with those of general Zn_2GeO_4.[32,33] The high-resolution N 1s XPS spectrum of Zn_2GeO_4/g-C_3N_4 hybrid could be deconvoluted into three peaks, as shown in Figure 4d. The peak at 399.9 eV can be attributed to the sp^3-bonded N atoms in $N(-C)_3$ or N atoms bonded with H atoms.[31] The two peaks at 399.3 and 398.8 eV correspond to N–O bonds and C–N=C, respectively.[31,34] The high-resolution XPS spectrum of C 1s (Figure 4e) can be deconvoluted into four peaks (centered at 284.8, 285.9, 288.3, and 289 eV), which correspond to reference C=C, C–O, sp^2-bonded C atoms in the g-C_3N_4 layers and C–N, respectively.[20,31,35]

The as-prepared samples were then assembled into Li half-cells to investigate their electrochemical performance. **Figure 5**a shows the cyclic voltammetry (CVs) curves of the Zn_2GeO_4/g-C_3N_{4-10}, which were collected at a slow scan rate of 0.05 mV s^{-1} for the first three cycles followed by a fast scan rate at 0.5 mV s^{-1} for the subsequent two cycles in a potential window of 0.01–3.0 V versus Li^+/Li. In the first cathodic process (discharge process), two sharp peaks at 0.75 and 1.15 V can be attributed to a multiple electrochemical reaction process, which includes the formation of solid electrolyte interface (SEI) layers and the decomposition of Zn_2GeO_4 into Zn, Ge, and Li_2O (Equation (5)).[19,36] Another small cathodic peak at 0.25 V indicates the alloying reactions of Li–Zn and Li–Ge (Equations (6) and (7)).[14,19] In the first charge process, two broad anodic peaks at 0.4 and 1.35 V can be assigned to the delithiation of Li-metal alloys (Equations (6) and (7)) and the reoxidation of metal (Equations (8) and (9)), respectively. Note that a pair of redox peaks located at about 1.55 and 2.4 V in

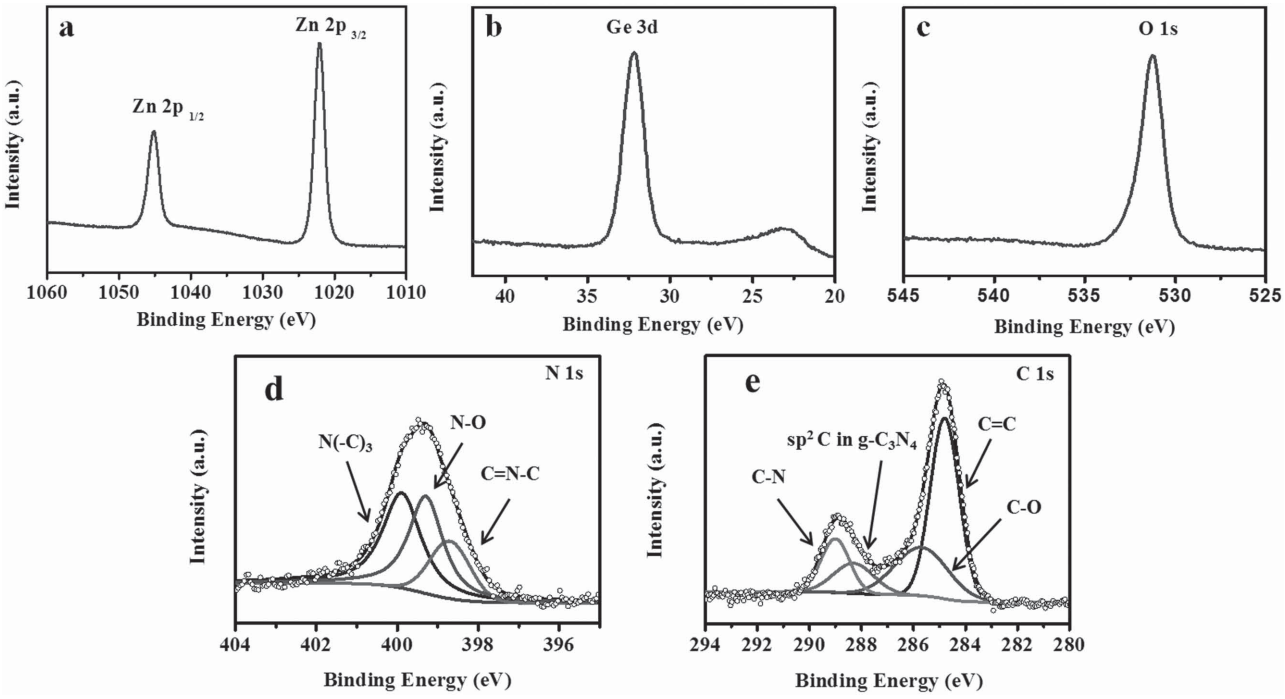

Figure 4. XPS spectra of Zn_2GeO_4/g-C_3N_{4-10}: a) Zn 2p peak, b) Ge 3d peak, c) O 1s peak, d) N 1s peak, and e) C 1s peak.

the CV curves of the Zn_2GeO_4/g-C_3N_4 hybrids and g-C_3N_4 does not appear in those of pure Zn_2GeO_4 (Figure 5c), which should result from the existence of g-C_3N_4 layers (Equation (10)). This pair of reversible peaks in pure g-C_3N_4 (Figure S2a, Supporting Information) is much weaker than those in Zn_2GeO_4/g-C_3N_4 hybrids even though the content of g-C_3N_4 in former is much higher than that in latter, indicating the synergistic lithium storage of Zn_2GeO_4/g-C_3N_4 hybrids. In the subsequent cycles, the main cathodic peak at about 0.75 V first shifts to about 0.9 V due to the irreversible decomposition of Zn_2GeO_4 and the new lithiation process of metal oxides. Then the main cathodic peak gradually shifts to low potentials, which is a common phenomenon in Zn_2GeO_4 anodes.[20,22] The peak shift is related to reversible degree of metal oxidation accompanied by the decomposition of Li_2O.[19] When the scan rate of CV measurements increases from 0.05 to 0.5 mV s^{-1}, the three pairs of well-defined anodic/cathodic peaks at 0.25/0.4, 0.75/1.35, and 1.55/2.4 V correspond to the reversible redox reactions of M/Li_yM (M = metal), M/MO_x, and C_3N_4/$Li_zC_3N_4$, respectively. Thus, the electrochemical reactions of the Zn_2GeO_4/g-C_3N_4 hybrids occur as follows

$$Zn_2GeO_4 + 8Li^+ + 8e^- \rightarrow 2Zn + Ge + 4Li_2O \quad (5)$$

$$Ge + xLi^+ + xe^- \leftrightarrows Li_xGe\,(0 \le x \le 4.4) \quad (6)$$

$$Zn + yLi^+ + ye^- \leftrightarrows Li_yZn\,(0 \le y \le 1) \quad (7)$$

$$Zn + Li_2O \leftrightarrows ZnO + 2Li^+ + 2e^- \quad (8)$$

$$Ge + 2Li_2O \leftrightarrows GeO_2 + 4Li^+ + 4e^- \quad (9)$$

$$C_3N_4 + zLi^+ + ze^- \leftrightarrows Li_zC_3N_4\,(0 \le z \le 4) \quad (10)$$

In order to better understand the lithium storage occurred in Zn_2GeO_4/g-C_3N_4 hybrids, a molecular structural region for initial Li-insertion process was demonstrated in **Scheme 1**. Large amounts of pyrrolic N "hole" defects with doubly bonded nitrogen exist in the natural structure of graphitic carbon nitride (g-C_3N_4) and the distance between two N "hole" defects on the g-C_3N_4 layers are about 7.13 Å.[28] The Li–N bond length is about 1.96 Å, and the distance between two Li atoms is 2.97 Å[37] according to Li bulk. Theoretically, Li tends to occupy the defects on g-C_3N_4 layers and the interlayers besides these two doubly bonded nitrogen atoms in g-C_3N_4 layers.[28] However, for experimentally reported bulky g-C_3N_4 anode,[38] these N "hole" defects on the g-C_3N_4 layers were barely exposed to electrolyte, thus Li reacted with a C_3N species on the g-C_3N_4 layers, which destroyed the crystallinity of g-C_3N_4 and resulted in low intercalation capacity and poor stability, as shown in Scheme 1a,b. In the as-prepared Zn_2GeO_4/g-C_3N_4 hybrids, Zn_2GeO_4 NPs are designed as spacers to isolate the ultrathin g-C_3N_4 layers from restacking, which enlarge the spacing distances but also increase the exposure of "hole" defects on the g-C_3N_4 layers (Scheme 1c). In this case, Zn_2GeO_4/g-C_3N_4 smart hybrids could provide more active sites for Li insertion and bring much larger Li adsorption energies at the defects,[25] leading to a low energy barrier for stable Li intercalation into defects (C_2N species), as shown in Scheme 1d. Meanwhile, these Zn_2GeO_4 NPs spacers would react with most Li^+ and be decomposed into Zn and Ge highly dispersed on the

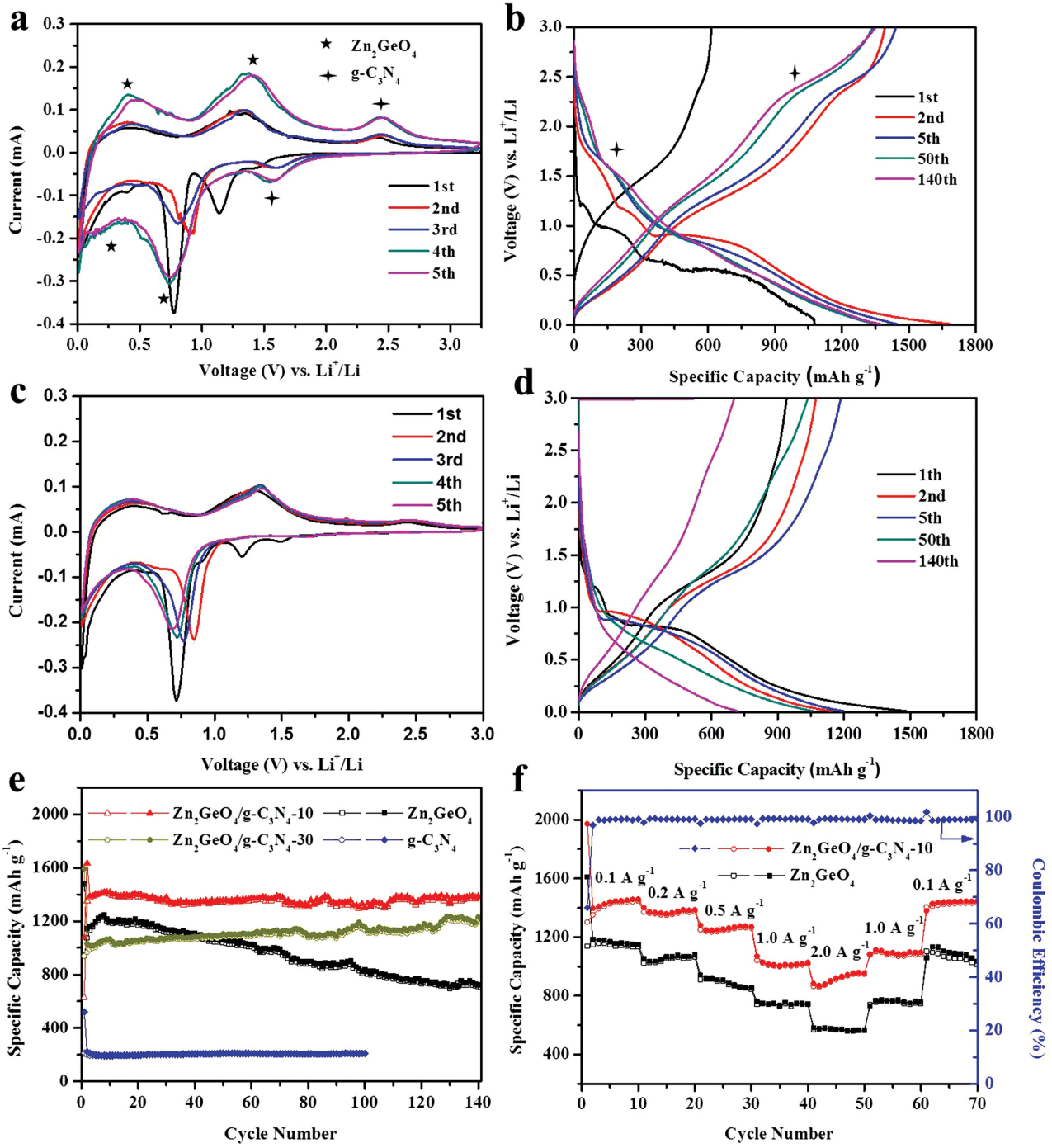

Figure 5. a) Representative C–V curve of the Zn_2GeO_4/g-C_3N_{4-10} for the first, second, and third cycles at a scan rate of 0.05 mV s^{-1} and fourth and fifth cycles at a scan rate of 0.5 mV s^{-1}; b) galvanostatic charge–discharge voltage profiles of the Zn_2GeO_4/g-C_3N_{4-10} at a current density of 200 mA g^{-1}; c) representative CV curve for the first, second, third, fourth, and fifth cycles of pure Zn_2GeO_4 nanoparticles at a scan rate of 0.05 mV s^{-1}; d) galvanostatic charge–discharge voltage profiles of pure Zn_2GeO_4 nanoparticles at a current density of 200 mA g^{-1}; e) comparative cycling performance of bare g-C_3N_4, pure Zn_2GeO_4 NPs, the Zn_2GeO_4/g-C_3N_{4-10}, and Zn_2GeO_4/g-C_3N_{4-30} at a current density of 200 mA g^{-1}; and f) rate performance of the Zn_2GeO_4/g-C_3N_{4-10} and pure Zn_2GeO_4 NPs at different current densities.

g-C_3N_4 layers, which largely enhance the electrical conductivity of the hybrids anode. Furthermore, the 2D structure of g-C_3N_4 layers could effectively accommodate the strain of the volume change of Zn_2GeO_4 NPs and prevent the formation of unstable SEI during cycling. The affinity between g-C_3N_4 layer and Zn_2GeO_4 NPs restrains the aggregation and pulverization of Zn_2GeO_4 upon lithiation/delithiation. The synergistic effect between Zn_2GeO_4 and g-C_3N_4 originating from the structural

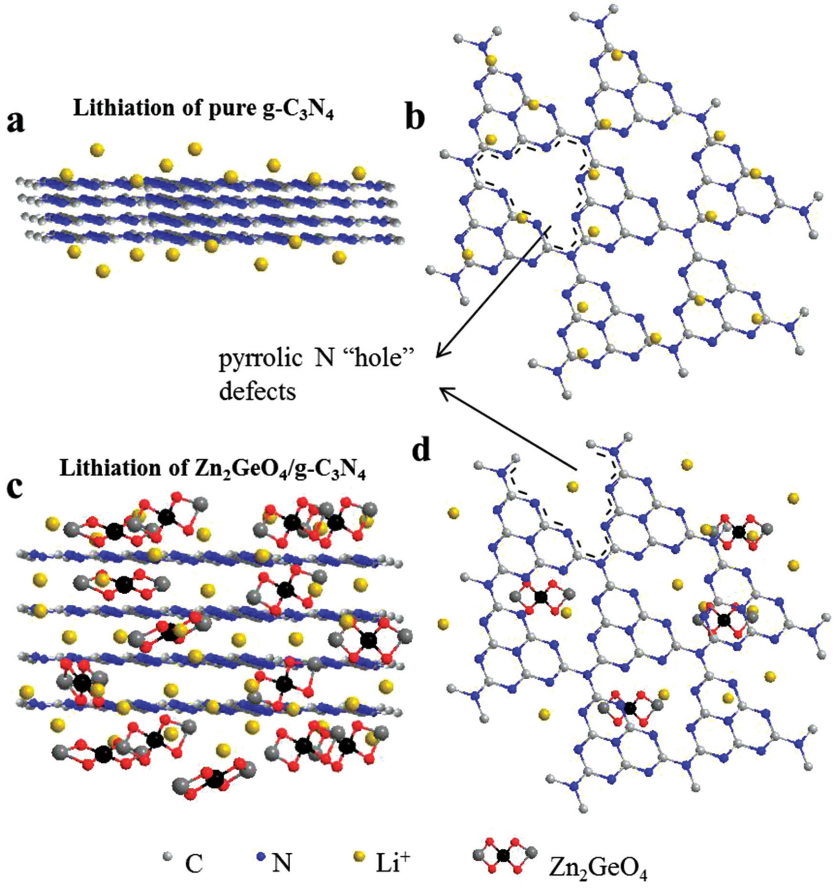

Scheme 1. Illustrations of pure a,b) g-C_3N_4 and c,d) Zn_2GeO_4/g-C_3N_4 hybrids for Li-insertion viewed from the a,c) edge and b,d) basal plan directions.

advantages of Zn_2GeO_4/g-C_3N_4 smart hybrids is expected to bring out excellent electrochemical performance.

Figure 5b presents the galvanostatic discharge–charge (GDC) voltage profiles of the Zn_2GeO_4/g-C_3N_{4-10} in the potential window of 0.001–3 V at a current density of 200 mA g^{-1}. Upon initial discharge, two apparent voltage plateaus at 1.5–0.5 V are attributed to the formation of SEI layers[21] and the decomposition of Zn_2GeO_4 into Zn, Ge, and Li_2O (Equation (1)), while the sloped profile at <0.5 V corresponds to the alloying process of Li–Zn and Li–Ge (Equations (6) and (7)). Compare to the GDC profiles of pure Zn_2GeO_4 and bare g-C_3N_4 layers (Figure 5d and Figure S2, Supporting Information), the reversible voltage plateaus at >1.5 V could be due to the lithiation of g-C_3N_4 layers (Equation (10)). These GDC results are well consistent with the CV results. Moreover, the initial discharge and charge specific capacities of Zn_2GeO_4/g-C_3N_{4-10} are 1068 and 626 mA h g^{-1}, respectively, leading to a Coulombic efficiency (CE) of 58.6%. The initial irreversible capacity loss could be ascribed to the formation of SEI and the incomplete reduction of Li_2O.[19,22] Note that the second discharge curve is very similar to the initial one, indicating that some reactions have not occurred timely, which is likely due to the slower activation process of Zn_2GeO_4/g-C_3N_{4-10} at 200 mA g^{-1}. After the first two cycles, the as-prepared Zn_2GeO_4/g-C_3N_{4-10} exhibits a highly reversible electrochemical performance, for example, the subsequent capacity fading of specific capacity is less than 5% from 2nd to 140th cycle. In contrast, pure Zn_2GeO_4 NPs exhibit normal initial discharge and charge specific capacities of 1479 and 941 mA h g^{-1} (Figure 5d), but relatively fast capacity fading with a value of as much as 40% from 2nd to 140th cycle. Therefore, the unique hybrid nanostructure of Zn_2GeO_4/g-C_3N_{4-10} could effectively accommodate the volume changes and maintain high reversible capacity, highlighting the synergistic effect between the two components of the hybrids.

The synergistically enhanced lithium storage of the Zn_2GeO_4/g-C_3N_4 hybrids is further demonstrated by the differentiated cycle behaviors of as-prepared samples, as shown in Figure 5e. During the 140 charging–discharging cycles, the specific capacity of Zn_2GeO_4/g-C_3N_{4-10} remains stably above 1300 mA h g^{-1} at the current density of 200 mA g^{-1}, and the CE quickly stabilizes at ≈99% from the second cycle (Figure S3a, Supporting Information). Zn_2GeO_4/g-C_3N_{4-30} shows lower initial specific capacity of 939 mA h g^{-1} but the specific capacity keeps increasing gradually, indicating longstanding activation process possibly due to the excess existence of g-C_3N_4. In contrast, the specific capacity of the bare Zn_2GeO_4 NPs decreases quickly from 1229 to 711 mA h g^{-1} at 200 mA g^{-1} after 140 cycles, and the CE is still around 98% from second cycle (Figure S3b, Supporting Information). Apparently, Zn_2GeO_4 NPs suffer from severe capacity degradation and unstable SEI formation upon charge–discharge cycling which can be attributed to the large volume change of Zn_2GeO_4 materials and the pulverization of Zn_2GeO_4 nanoparticles, causing electrical disconnection from current collectors during lithium ion insertion and extraction. The bare g-C_3N_4 layers deliver specific capacities of 200 mA h g^{-1} at 200 mA g^{-1} with rapid stabilization of CE at >99% (Figure S3c, Supporting Information). The low specific capacity of bare g-C_3N_4 layers may be due to the aggregation of layers without the anchorage force of nanoparticles. But the cycling stability of g-C_3N_4 layers demonstrates the potential advantage of g-C_3N_4 as fine substrate matrix for lithium storage. In summary, according to these cycle behaviors, the lithium storage capacity of Zn_2GeO_4/g-C_3N_{4-10} exceeds that of either individual component, demonstrating the synergistic capacity enhancement. Besides the improved cycling performance, the Zn_2GeO_4/g-C_3N_4 hybrids show outstanding rate capability (Figure 5f). Even at 2000 mA g^{-1}, Zn_2GeO_4/g-C_3N_{4-10} still delivers a high specific capacity of 950 mA h g^{-1}, whereas pure Zn_2GeO_4 NPs can only deliver the capacity of 520 mA h g^{-1} at the same current density. When the current density is recovered to 100 mA g^{-1}, the reversible capacity of Zn_2GeO_4/g-C_3N_{4-10} returns to 1400 mA h g^{-1} immediately, revealing the good capacity recovery and stable composite structure.

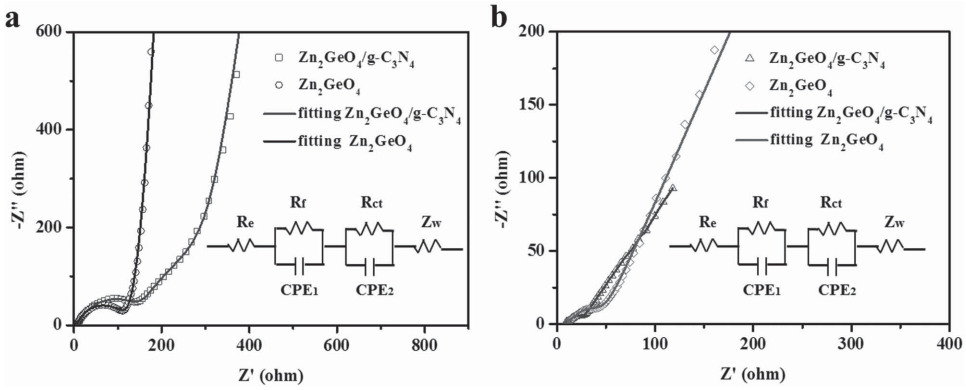

Figure 6. Electrochemical impedance spectra (100 kHz to 100 mHz) of Zn_2GeO_4/g-C_3N_{4-10} and pure Zn_2GeO_4 NPs: a) before cycling and b) after 140 cycles at the delithiation state. Two insets are the corresponding equivalent circuits.

Table 1. Kinetic parameters of Zn_2GeO_4/g-C_3N_{4-10} and pure Zn_2GeO_4 NPs anodes before and after cycling.

Samples	Voltage [V]	R_f [Ω]	R_{ct} [Ω]
Fresh Zn_2GeO_4	3.29	96.1	104.7
Fresh hybrids	2.99	153	136.1
Postcycled Zn_2GeO_4	2.2	4.3	33.7
Postcycled hybrids	2.39	7.6	8.5

Electrochemical impedance measurements of Zn_2GeO_4/g-C_3N_{4-10} and pure Zn_2GeO_4 anodes were carried out to understand the charge transfer in the fresh and cycled cells. A whole Nyquist plot is composed of one semicircle at the high and medium frequency zone, followed by a slope line at the low-frequency region. The high-frequency zone is a representation of contact resistance (R_f), and the medium frequency semicircular can be explained as the charge-transfer resistance (R_{ct}) of the electrode/electrolyte interface, while the low-frequency sloping straight line is equivalent to the Warburg impedance (Z_w), corresponding to the solid-state diffusion of lithium ions in the bulk electrode (R_e). Therefore, an equivalent circuit can be applied to analyze the impendence spectra (**Figure 6**), and the fitting results are given in **Table 1**. As displayed in Figure 6a, Zn_2GeO_4/g-C_3N_{4-10} shows a larger semicircle diameter compared to pure Zn_2GeO_4 NPs before cycling due to the unactivated g-C_3N_4 layers for lithium storage, resulting in a higher charge transfer resistance. After repeated lithiation/delithiation processes, the Zn_2GeO_4 NPs decomposed into well-dispersed metal/metal oxide nanoparticles on ultrathin g-C_3N_4 layers, sharply decreasing the charge transfer resistance of Zn_2GeO_4/g-C_3N_4 hybrids anode. In the subsequent charge/discharge processes, large-area g-C_3N_4 layers could suppress the volume change, pulverization, and aggregation of these nanoparticles, and hence charge-transfer resistance R_{ct} (8.5 Ω) of the Zn_2GeO_4/g-C_3N_4 hybrid is much smaller than that (33.7 Ω) of Zn_2GeO_4 NPs after 140 cycles.

Table 2 summarizes all the recent works on the Zn_2GeO_4 based composite as anodes for lithium-ion batteries. The specific capacity of Zn_2GeO_4/g-C_3N_4 hybrids in this work is the highest among the reported values for Zn_2GeO_4 based composite at similar current densities. Besides the high capacity, Zn_2GeO_4/g-C_3N_4 hybrids also exhibit excellent rate capability and cycling stability. The outstanding electrochemical performance of Zn_2GeO_4/g-C_3N_4 hybrids can be attributed to its unique hybrid architecture and synergistic effects between the constituents of the composite. First, Zn_2GeO_4 nanoparticles contribute to high specific capacity and act as spacers to expand the interlayers of g-C_3N_4 layer for extra Li-ion storage and diffusion pathway. Meanwhile, the isolated ultrathin g-C_3N_4 expose more abundant pyrrolic N "hole" defects, which further contribute high capacity to the hybrids electrode. Second, metal Zn and Ge, arising from decomposition of Zn_2GeO_4 after the first lithiation, are highly dispersed on the g-C_3N_4 layers, which largely enhance the electrical conductivity of the hybrid nanostructures. Finally, the large-area g-C_3N_4 layers could effectively accommodate the strain of the volume change of active materials and restrain the aggregation and pulverization of nanoparticles upon lithiation/delithiation. Therefore,

Table 2. Comparison of electrochemical cycling and rate performance of Zn_2GeO_4 based anode materials.

Anode materials	Capacity after 100 cycles	Rate performance	ref.
Zn_2GeO_4/N-doped graphene	1044 mA h g^{-1} @ 400 mA g^{-1}	909, 846, 773, 678, 531 mA h g^{-1} @ 0.2, 0.4, 0.8, 1.6, 3.2 A g^{-1}	[19]
Amorphous Zn_2GeO_4 nanoparticles	1000 mA h g^{-1} @ 400 mA g^{-1}	860, 810, 700, 610, 470 mA h g^{-1} @ 0.4, 0.8, 1.6, 3.2, 6.4 A g^{-1}	[14]
Zn_2GeO_4/graphene oxide	1150 mA h g^{-1} @ 200 mA g^{-1}	1096, 1009, 896, 736, 538 mA h g^{-1} @ 0.2, 0.4, 0.8, 1.6, 3.2 A g^{-1}	[18]
Zn_2GeO_4 nanorods	616 mA h g^{-1} @ 400 mA g^{-1}	700, 600, 530, 480 mA h g^{-1} @ 0.4, 0.8, 1.6, 4 A g^{-1}	[15]
Zn_2GeO_4 nanowires/carbon textiles	1080 mA h g^{-1} @ 400 mA g^{-1}	800, 500, 400, 280, 200 mA h g^{-1} @ 0.4, 1, 2, 5, 8 A g^{-1}	[33]
Zn_2GeO_4/g-C_3N_4 hybrids	1304 mA h g^{-1} @ 200 mA g^{-1}	1433, 1355, 1243, 1004, 947 mA h g^{-1} @ 0.1, 0.2, 0.5, 1.0, 2.0 A g^{-1}	This work

Zn_2GeO_4/g-C_3N_4 hybrids demonstrate enhanced kinetic performance, cycling stability, and improved conductivity and Coulombic efficiency, highlighting the synergistic effect.

3. Conclusions

In summary, smart hybrids of Zn_2GeO_4 NPs and ultrathin g-C_3N_4 layers have been successfully developed by a simple and cost-effective low-temperature solution method. As the anode materials for LIBs, the cooperation of the two active components in the Zn_2GeO_4/g-C_3N_4 hybrids generates a synergistic enhanced effect on the electrochemical lithium storage. The 2D g-C_3N_4 layers effectively accommodate the volume changes and prevent the formation of unstable SEI, while monodisperse Zn_2GeO_4 NPs prevent ultrathin g-C_3N_4 layers from restacking, promote lithiation/delithiation kinetics, and contribute to the high specific capacities. As the anode materials for LIBs, the well-designed Zn_2GeO_4/g-C_3N_4 hybrids exhibit a high charge capacity of 1370 mA h g^{-1} at 200 mA g^{-1} after 140 cycles. The Zn_2GeO_4/g-C_3N_4 hybrids also display an excellent rate performance (950 mA h g^{-1} at 1000 mA g^{-1}), making it a promising anode material for high-performance LIBs.

4. Experimental Section

Raw Materials: The chemicals were used as received without further purification process. They include GeO_2 (purity ≥99.99%, trace metals basis, Sigma-Aldrich, Australia), dicyandiamide ($C_2H_4N_4$) (purity ≥99.99%, Sigma-Aldrich, Australia), Na_2CO_3 (purity ≥99.99%, Sigma-Aldrich, Australia), $Zn(CH_3COO)_2{\cdot}2H_2O$ (purity ≥99.99%, Sigma-Aldrich, Australia), 1-methyl-2-pyrrolidone (NMP) (purity ≥99%, Sigma-Aldrich, Australia), polyimide (PI) (Sigma-Aldrich, Australia) and hydrochloric acid (HCl) (ACS reagent, 37%, Sigma-Aldrich, Australia).

Preparation of g-C_3N_4: Bulky g-C_3N_4 was prepared by heating dicyandiamide to 550 °C with a ramp rate of 2.3 °C min^{-1} for 4 h under static air.[31] To protonate the obtained bulk g-C_3N_4, 1 g of such material was vigorously stirred in 25 mL of 10 M HCl for 1 h at room temperature. The mixture was washed via centrifugation repeatedly to remove the superfluous HCl. And then the protonated g-C_3N_4 was dried at 60 °C until further use.

Synthesis of Zn_2GeO_4/g-C_3N_4 Hybrids: 10 or 30 mg protonated g-C_3N_4 was ultrasonicated in 10 mL DI water for 2 h to obtain g-C_3N_4 layer followed by the addition of 219 mg $Zn(CH_3COO)_2{\cdot}2H_2O$. Such mixture was further ultrasonicated for another 2 h (labeled as solution A); meanwhile, 83 mg Na_2GeO_3 (Na_2GeO_3 solid powder was prepared by heating stoichiometric mixture of Na_2CO_3 and GeO_2 at 900 °C for 12 h) was dissolved in 10 mL DI water (labeled as solution B). And then, solution B was added into solution A and the mixture was vigorously stirred at 100 °C for 3 h. Then, the mixture was washed by ethanol and DI water and dried in oven at 80 °C. The as-prepared hybrids with addition of 10 and 30 mg g-C_3N_4 were named as Zn_2GeO_4/g-C_3N_{4-10} and Zn_2GeO_4/g-C_3N_{4-30}, respectively. For comparison, pure Zn_2GeO_4 nanoparticles were prepared according to the same method as mentioned above, except for the addition of g-C_3N_4 layers.

Characterization: The distribution, size, and morphology of the as-prepared samples were characterized by scanning electron microscopy (SEM) (Magellan SEM, FEI, USA). TEM and HRTEM measurements were conducted on a Zeiss Libra 200FE microscope. The chemical compositions and structures of the as-prepared samples were analyzed by XRD (Bruker D8 Advance X-ray diffractometer, Cu Kα radiation r = 0.15406 nm) and XPS (AXIS Ultra-DLD, Kratos Analytical, Manchester, UK, using monochromated Al Ka radiation).

Electrochemical Measurements: The working electrodes were fabricated by coating a slurry containing 70 wt% of active materials (Zn_2GeO_4/g-C_3N_4 hybrids, Zn_2GeO_4 NPs, or g-C_3N_4), 20 wt% of acetylene black (Super-P), and 10 wt% of PI dissolved in *N*-methyl-2-pyrrolidinone onto a copper foil and dried at 60 °C for 4 h in a vacuum (10^{-3} Torr). Then the samples were sintered in Ar at 300 °C for 2 h with the heating rate of 10 °C min^{-1} and dried at 100 °C in vacuum for 12 h before pressing. Standard CR2032-type coin cells were assembled in an Ar-filled glovebox (KIYON, Korea) by using the as-prepared anode, Li metal foil (0.4 mm thick) as the counter electrode, and a separator (Solupor 7P03A). The electrolyte was 1 M $LiPF_6$ dissolved in a mixture of ethylene carbonate (EC) and dimethyl carbonate (DMC) (v/v = 1:1). The cells were aged for 12 h prior to the electrochemical measurements. GDC experiments were performed at different current densities in the voltage window of 0.01–3.00 V with a multichannel battery tester (Maccor, Inc., USA). CV measurements were conducted by using an electrochemical workstation (Solartron Potentiostat and Impedance Analyser, UK). Electrochemical impedance spectra (EIS) were recorded using the same electrochemical workstation by applying an AC voltage of 10 mV amplitude over the frequency range from 100 kHz to 100 mHz. The battery GDC cycling and rate tests were performed with a mass loading of active electrode materials of ≈0.85 mg cm^{-2}.

Supporting Information

Supporting Information is available from the Wiley Online Library or from the author.

Acknowledgements

This work was supported partially by National High-tech R&D Program of China (863 Program, No. 2015AA034601), National Natural Science Foundation of China (Grant Nos. 91333122, 51402106, 51372082, 51172069, 50972032, 61204064, and 51202067), Ph.D. Programs Foundation of Ministry of Education of China (Grant Nos. 20110036110006, 20120036120006, and 20130036110012), Par-Eu Scholars Program, and the Fundamental Research Funds for the Central Universities. W.L. acknowledges financial support of Marie-Curie COFUND program (NanoTrainforGrowth). XD.L and Y.F specially thank Prof. Huanting Wang from Monash University for his discussion.

Received: July 16, 2015
Revised: September 2, 2015
Published online: October 13, 2015

[1] N. S. Choi, Z. Chen, S. A. Freunberger, X. Ji, Y. K. Sun, K. Amine, G. Yushin, L. F. Nazar, J. Cho, P. G. Bruce, *Angew. Chem. Int. Ed.* **2012**, *51*, 9994.
[2] M. Armand, J.-M. Tarascon, *Nature* **2008**, *451*, 652.
[3] B. Dunn, H. Kamath, J.-M. Tarascon, *Science* **2011**, *334*, 928.
[4] J. B. Goodenough, K.-S. Park, *J. Am. Chem. Soc.* **2013**, *135*, 1167.
[5] N. A. Kaskhedikar, J. Maier, *Adv. Mater.* **2009**, *21*, 2664.
[6] C. K. Chan, H. Peng, G. Liu, K. McIlwrath, X. F. Zhang, R. A. Huggins, Y. Cui, *Nat. Nanotechnol.* **2008**, *3*, 31.
[7] H. Kim, Y. Son, C. Park, J. Cho, H. C. Choi, *Angew. Chem. Int. Ed.* **2013**, *125*, 6113.
[8] X.-L. Wang, W.-Q. Han, H. Chen, J. Bai, T. A. Tyson, X.-Q. Yu, X.-J. Wang, X.-Q. Yang, *J. Am. Chem. Soc.* **2011**, *133*, 20692.
[9] Y. S. Hu, R. Demir-Cakan, M. M. Titirici, J. O. Müller, R. Schlögl, M. Antonietti, J. Maier, *Angew. Chem. Int. Ed.* **2008**, *47*, 1645.
[10] K. H. Seng, M.-H. Park, Z. P. Guo, H. K. Liu, J. Cho, *Nano Lett.* **2013**, *13*, 1230.

[11] J. Graetz, C. Ahn, R. Yazami, B. Fultz, *J. Electrochem. Soc.* **2004**, *151*, A698.
[12] D. KeeáYi, *Energy Environ. Sci.* **2012**, *5*, 9028.
[13] W. Li, Y.-X. Yin, S. Xin, W.-G. Song, Y.-G. Guo, *Energy Environ. Sci.* **2012**, *5*, 8007.
[14] R. Yi, J. Feng, D. Lv, M. L. Gordin, S. Chen, D. Choi, D. Wang, *Nano Energy* **2013**, *2*, 498.
[15] J. Feng, M. Lai, L. Lu, *Electrochem. Commun.* **2011**, *13*, 287.
[16] F. Zhang, R. Zhang, Z. Zhang, H. Wang, J. Feng, S. Xiong, Y. Qian, *Electrochim. Acta* **2014**, *150*, 211.
[17] Z. Chen, Y. Yan, S. Xin, W. Li, J. Qu, Y.-G. Guo, W.-G. Song, *J. Mater. Chem. A* **2013**, *1*, 11404.
[18] S. J. Yang, S. Nam, T. Kim, J. H. Im, H. Jung, J. H. Kang, S. Wi, B. Park, C. R. Park, *J. Am. Chem. Soc.* **2013**, *135*, 7394.
[19] F. Zou, X. Hu, L. Qie, Y. Jiang, X. Xiong, Y. Qiao, Y. Huang, *Nanoscale* **2014**, *6*, 924.
[20] F. Zou, X. Hu, Y. Sun, W. Luo, F. Xia, L. Qie, Y. Jiang, Y. Huang, *Chem. - Eur. J.* **2013**, *19*, 6027.
[21] W. Chen, L. Lu, S. Maloney, Y. Yang, W. Wang, *Phys. Chem. Chem. Phys.* **2015**, *17*, 5109.
[22] R. Wang, S. Wu, Y. Lv, Z. Lin, *Langmuir* **2014**, *30*, 8215.
[23] X. Li, W. Li, M. Li, P. Cui, D. Chen, T. Gengenbach, L. Chu, H. Liu, G. Song, *J. Mater. Chem. A* **2015**, *3*, 2762.
[24] S. Jin, C. Wang, *Nano Energy* **2014**, *7*, 63.
[25] X. Wang, Q. Weng, X. Liu, X. Wang, D.-M. Tang, W. Tian, C. Zhang, W. Yi, D. Liu, Y. Bando, D. Golberg, *Nano Lett.* **2014**, *14*, 1164.
[26] Y. Zhang, A. Thomas, M. Antonietti, X. Wang, *J. Am. Chem. Soc.* **2009**, *131*, 50.
[27] M. Wu, Q. Wang, Q. Sun, P. Jena, *J. Phys. Chem. Lett. C* **2013**, *117*, 6055.
[28] H. Pan, *J. Phys. Chem. Lett. C* **2014**, *118*, 9318.
[29] Y. Gong, M. Li, Y. Wang, *ChemSusChem* **2015**, *8*, 931.
[30] X. Zhang, X. Xie, H. Wang, J. Zhang, B. Pan, Y. Xie, *J. Am. Chem. Soc.* **2013**, *135*, 18.
[31] T. Y. Ma, S. Dai, M. Jaroniec, S. Z. Qiao, *Angew. Chem. Int. Ed.* **2014**, *53*, 7281.
[32] L. Sun, Y. Qi, C.-J. Jia, Z. Jin, W. Fan, *Nanoscale* **2014**, *6*, 2649.
[33] Q. Liu, Y. Zhou, Z. Tian, X. Chen, J. Gao, Z. Zou, *J. Mater. Chem.* **2012**, *22*, 2033.
[34] R. Asahi, T. Morikawa, *Chem. Phys.* **2007**, *339*, 57.
[35] Y. Xue, J. Liu, H. Chen, R. Wang, D. Li, J. Qu, L. Dai, *Angew. Chem. Int. Ed.* **2012**, *51*, 12124.
[36] W. Chen, L. Lu, S. Maloney, Y. Yang, W. Wang, *Phys. Chem. Chem. Phys.* **2015**, *17*, 5109.
[37] J.-H. Cho, S.-H. Ihm, M.-H. Kang, *Phys. Rev. B* **1993**, *47*, 14020.
[38] G. M. Veith, L. Baggetto, L. A. Adamczyk, B. Guo, S. S. Brown, X.-G. Sun, A. A. Albert, J. R. Humble, C. E. Barnes, M. J. Bojdys, S. Dai, N. J. Dudney, *Chem. Mater.* **2013**, *25*, 503.